Optimizing Defect Detection in Mild Steel Using Colour Temperature Control in Infrared Thermography

by Suresh Kumar Bhambhu*, Vanita Arora**, Shruti Bharadwaj*** and Ravibabu Mulaveesala*

* *InfraRed Imaging Laboratory (IRIL), Centre for Sensors, Instrumentation and Cyber Physical System Engineering (SeNSE), Indian Institute of Technology Delhi, Hauz Khas, New Delhi, INDIA 110016*

** *InfraRed Vision & Automation Pvt. Limited, Ward No 08, Sun City, Rup Nagar, Punjab, India,140001*

*** *Computational InfraRed Imaging Laboratory (CIRIL), Centre for Sensors, Instrumentation and Cyber Physical System Engineering (SeNSE), Indian Institute of Technology Delhi, Hauz Khas, New Delhi, INDIA 110016*

Abstract

Active infrared thermography is strongly influenced by the spectral characteristics of the excitation source and the resulting transient thermal response within the inspected material. This study investigates the influence of correlated colour temperature (CCT) of LED excitation sources on pulsed thermographic inspection of a mild steel specimen containing controlled subsurface material loss. Systematic variation of CCT from 2800 K to 6000 K revealed a monotonic increase in heating-phase slope by 37.9% and progressively steeper cooling behaviour by 42.1%, providing quantitative evidence that CCT systematically influences absorbed thermal energy. Cross-Correlation Coefficient processing consistently produced superior defect representation compared to phase-based approaches.

1. Introduction

Non-destructive testing plays a critical role in ensuring the structural integrity and reliability of engineering components across aerospace, power generation, manufacturing, and civil infrastructure, where early detection of subsurface defects prevents catastrophic failure and reduces maintenance costs. Among the wide range of NDT techniques available, active infrared thermography has established itself as a particularly powerful inspection modality, offering rapid whole-field, non-contact operation with the capability to detect both surface and subsurface anomalies through spatially and temporally resolved measurement of thermally induced surface temperature evolution [1], [2], [3].

In pulsed thermography (PT), a controlled thermal stimulus is applied to the specimen surface, and the resulting transient temperature evolution is monitored using a calibrated infrared camera. Subsurface defects disturb local heat flow, producing detectable thermal contrast signatures at the surface [4], [5], [6].

Extensive research has addressed PT optimisation through excitation power management, pulse duration selection, and post-processing algorithm development. Signal processing approaches, including Frequency Domain Phase (FDP), Time Domain Phase (TDP), and correlation-based Cross-Correlation Coefficient (CCC) methods, have been developed to enhance defect-related signatures and suppress background thermal noise. One important excitation parameter that has received comparatively limited systematic investigation is the spectral characteristic of the excitation source, represented by its correlated colour temperature (CCT)[7], [8], [9], [10].

The correlated colour temperature (CCT) of a light source is a colourimetric descriptor defined as the temperature of the Planckian blackbody radiator whose chromaticity most closely matches that of the source's output. In LED-based thermographic systems, which have gained considerable traction owing to energy efficiency, precise controllability, long operational lifetime, and spectrally tunable output, CCT can be systematically varied without altering the total emitted optical power. Variations in correlated colour temperature modify the spectral characteristics of the excitation source and consequently influence the thermal energy absorbed at the specimen surface. Since the surface absorptance of engineering materials depends on wavelength, changes in CCT can alter thermal energy coupling and the resulting thermographic response behaviour. Consequently, CCT is a practically controllable excitation parameter that can influence transient thermal diffusion and defect visibility during PT inspection.

Despite this physically well-motivated mechanism, no systematic study has isolated and quantified the effect of CCT on PT defect detection in metallic specimens under controlled experimental conditions where all other parameters are held constant. Existing investigations of LED-based thermographic systems have addressed illumination uniformity, duty cycle optimisation, and energy efficiency, but have not treated the spectral dimension of excitation as an independently controllable inspection variable. This gap is significant given that modern LED driver technology permits real-time CCT tuning at no additional cost or system complexity, making CCT an immediately exploitable degree of freedom in practical inspection system design.

The present investigation directly addresses this gap. A cylindrical mild steel specimen containing a single artificial subsurface defect with depth varying continuously from 1 mm to 4 mm along the circumferential direction was subjected to PT excitation with CCT varied across five discrete settings of 2800 K, 3600 K, 4400 K, 5200 K, and 6000

License: https://creativecommons.org/licenses/by/4.0/deed.en

K, with all other experimental parameters held constant throughout. Thermal sequences were processed using FDP, TDP, and CCC, and evaluated using best-contrast thermogram analysis, SPP temporal analysis, and a novel dual-phase slope analysis applied to the heating phase (frames 0–1500) and the cooling phase (frames 1500–3000). The dual-phase slope framework, which has not previously been reported in the PT literature, enables simultaneous characterisation of CCT-dependent surface energy absorption during excitation and CCT-dependent thermal energy dissipation following excitation, providing a more complete quantitative picture of the CCT thermography interaction than single-phase analysis alone.

The primary contributions of this paper are: quantitative establishment of CCT as a governing parameter of surface thermal absorption in LED-based PT, introduction of dual-phase slope analysis as a metric for PT assessment, identification of a tendency toward saturation in thermal-response variation at higher CCT conditions for mild steel specimens, and demonstration of CCC superiority over phase-based processing across the investigated CCT range.

2. Theoretical and experimental framework

The temperature distribution within a solid medium subjected to external thermal excitation is governed by the three-dimensional Fourier heat conduction equation given in Eq. (1)[11], [12]:

$$\frac{\partial T(x,y,z,t)}{\partial t} = \alpha\left(\frac{\partial^2 T}{\partial x^2} + \frac{\partial^2 T}{\partial y^2} + \frac{\partial^2 T}{\partial z^2}\right) \quad (1)$$

where $T(x,y,z,t)$ represents the temperature field and $\alpha = k/\rho c_p$ denotes the thermal diffusivity of the material, with k(W/m·K), ρ(kg/m^3), and c_p(J/kg·K) denoting thermal conductivity, mass density, and specific heat capacity, respectively. For active thermographic inspection, heat transfer is predominantly along the depth direction; therefore, a one-dimensional approximation is considered in the present analysis. Under pulsed thermal excitation, the resulting transient heat diffusion governs the temporal evolution of the measured surface temperature response.

2.1. Pulsed thermography

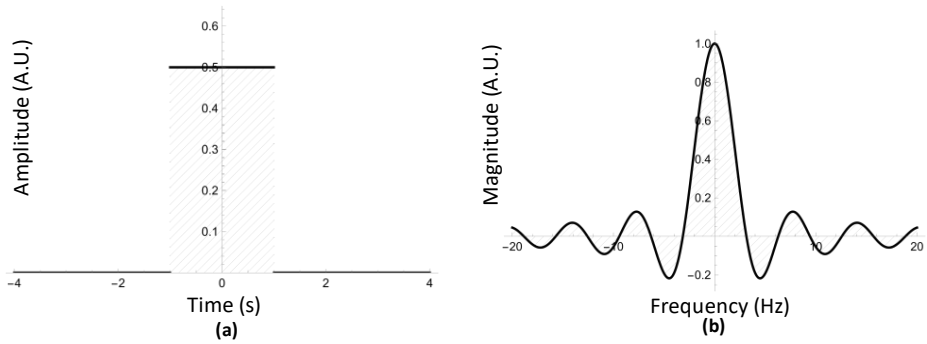

Figure 1. Theoretical framework of pulsed thermography (PT): (a) idealised pulse excitation waveform, and (b) corresponding broadband Fourier spectrum.

In PT, the specimen surface is subjected to a short-duration high-energy thermal pulse, approximated as an impulse excitation given in Eq. (2)[13], [14].

$$q(t) = Q_0\,\delta(t) \quad (2)$$

where Q_0 denotes the absorbed thermal energy per unit area (J/m²) and $\delta(t)$ represents the Dirac delta function. The corresponding one-dimensional transient temperature distribution for PT is expressed in Eq. (3) as

$$T(z,t) = \frac{Q_0}{\sqrt{4\pi\alpha t}}\,exp\left(-\frac{z^2}{4\alpha t}\right) \quad (3)$$

where z is the depth coordinate, and t is time after excitation. At the surface (z=0), this reduces to $t^{-1/2}$, indicating continuous monotonic decay. The transient pulse inherently contains a broad spectrum of thermal frequencies, enabling simultaneous interaction with defects at multiple depths. The associated thermal diffusion length at frequency f is given in Eq. (4):

$$\mu = \sqrt{\frac{\alpha}{\pi f}} \quad (4)$$

where lower frequencies correspond to greater penetration depth and higher frequencies interact primarily with near-surface features. In experiments, the LED source delivers a finite-duration pulse of absorbed heat flux. Q_0 over duration τ_p, approximating the impulse of Eq. (2) when τ_p is small relative to the characteristic thermal diffusion

time. The temporal profile and broadband Fourier spectrum of the excitation are shown in figure 1(a) and figure 1(b) respectively. The acquired thermal data are represented as a continuous sequence $T(x,y,t), t \in [0, T_{obs}]$, where x and y are spatial coordinates on the specimen surface and T_{obs} is the total observation duration.

3. Signal processing framework

The acquired thermal sequences were processed using three post-processing approaches: FDP, TDP, and CCC. Each method extracts defect-related thermal signatures through distinct signal-processing mechanisms, enabling comparative evaluation of defect characterisation capability under pulsed thermographic excitation. In all cases, the zero-mean thermal sequence $T'(x,y,t)$ defined in Eq. (5) serves as the common input to the processing pipeline. The complete signal-processing workflow, from thermal data acquisition through zero-mean preprocessing to FDP, TDP, and CCC processing, is summarised in figure 2 [15].

3.1. Zero-mean thermal response pre-processing

Prior to signal processing, zero-mean preprocessing was applied to suppress slowly varying background temperature variations. The zero-mean thermal response is expressed as Eq. (5):

$$T'(x,y,t) = T(x,y,t) - \frac{1}{T_{obs}} \int_0^{T_{obs}} T(x,y,t)\ dt \qquad (5)$$

where T_{obs} denotes the total observation duration. The resulting zero-mean sequence was used for FDP, TDP, and CCC processing.

3.2. Frequency domain phase analysis (FDP)

The FDP approach extracts phase information from the thermal response in the frequency domain through frequency decomposition. For each pixel location (x,y), the Fourier transform of the zero-mean thermal sequence is computed as expressed in Eq. (6):

$$F(x,y,\omega) = \int_0^{T_{obs}} T'(x,y,t)\, exp(-j\omega t)\ dt \qquad (6)$$

where ω denotes the continuous angular frequency variable, and T_{obs} is the total observation duration defined in (8). The complex Fourier spectrum is decomposed as in Eq. (7):

$$F(x,y,\omega) = F_R(x,y,\omega) + jF_I(x,y,\omega) \qquad (7)$$

where F_R and F_I represent the real and imaginary spectral components, respectively. The corresponding phase distribution is given in Eq. (8) as:

$$\phi(x,y,\omega) = tan^{-1}\left(\frac{F_I(x,y,\omega)}{F_R(x,y,\omega)}\right) \qquad (8)$$

The FDP approach suppresses slowly varying thermal backgrounds through Fourier decomposition and extracts phase information from individual frequency components of the transient thermal response. Since pulsed thermography inherently contains a broad spectrum of thermal frequencies, the resulting phase behaviour evolves continuously throughout the observation period.

3.3. Time domain phase analysis (TDP)

The TDP approach extracts instantaneous phase information directly from the temporal thermal response using analytic signal representation [16], [17]. The analytic signal constructed from the zero-mean thermal response is expressed in Eq. (9):

$$Z(x,y,t) = T'(x,y,t) + j\hat{T}(x,y,t) \qquad (9)$$

where $\hat{T}(x,y,t)$ represents the Hilbert transform of $T'(x,y,t)$, expressed in Eq. (10):

$$\hat{T}(x,y,t) = \frac{1}{\pi}\ \text{P.V.} \int_{-\infty}^{\infty} \frac{T'(x,y,\tau)}{t-\tau}\ \mathrm{d}t \qquad (20)$$

where P.V. denotes the Cauchy principal value of the integral, the instantaneous phase distribution obtained from the analytic signal is given in Eq. (11) as:

$$\phi(x,y,t) = tan^{-1}\left(\frac{\hat{T}(x,y,t)}{T'(x,y,t)}\right) \qquad (31)$$

Unlike FDP, the TDP approach preserves the full temporal phase evolution directly in the time domain. Consequently, the transient thermal response under pulsed thermography produces continuously evolving instantaneous phase profiles throughout the observation period, enabling temporal characterisation of defect-induced thermal behaviour.

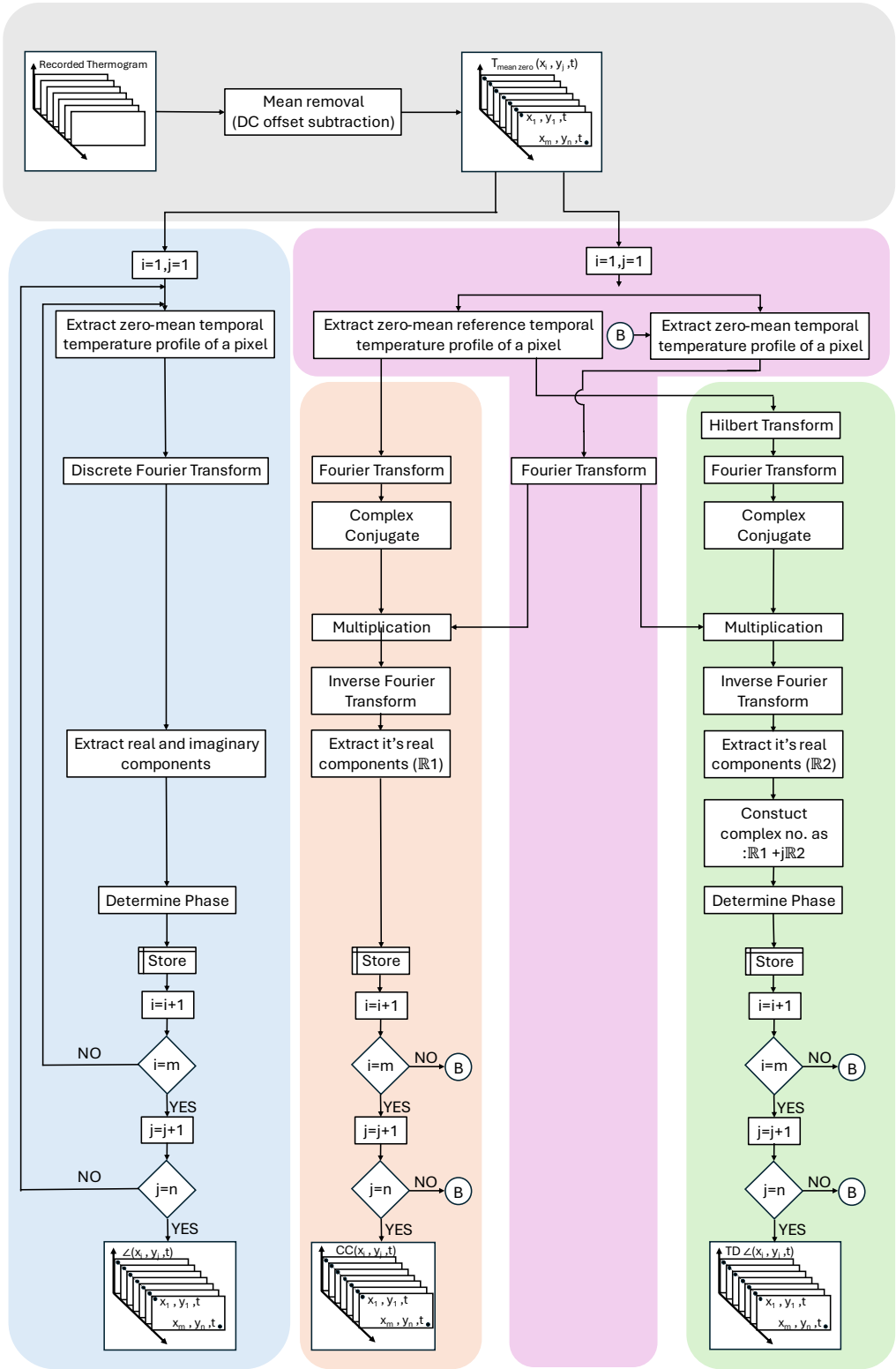

Figure 2. Signal-processing workflow employed for thermographic data analysis, including thermal data acquisition, zero-mean pre-processing, FDP, TDP and CCC post-processing.

3.4. Cross-correlation coefficient (CCC)

To evaluate the similarity between the applied excitation signal and the measured thermal response at each spatial location, cross-correlation analysis was performed. Let s(t) denote the continuous excitation sequence and $T'(x,y,t)$ denote the corresponding zero-mean thermal response. The cross-correlation coefficient is expressed in Eq.(12) [18], [19], [20], [21]:

$$C(x,y) = \int_0^{T_{obs}} s(t)\ T'(x,y,t)\ dt \qquad (42)$$

The CCC accumulates the continuous point-wise product of the excitation signal $s(t)$ and the zero-mean thermal response $T'(x,y,t)$ over the full observation duration T_{obs}, producing a spatial map of excitation-response agreement. Pixel locations exhibiting strong thermal response in phase with the excitation yield large positive values in (17), whereas regions with weak or incoherent thermal response yield values approaching zero. Consequently, defect-induced thermal perturbations, which modify the local correlation structure between excitation and response, become more distinguishable under PT excitation conditions.

It is noted that in practice, the continuous integrals in Eq.(5), Eq.(6), and Eq.(12) are evaluated numerically using the acquired discrete thermal sequences at a sampling rate of $f_s = 30$ Hz over N temporal samples, where $N = f_s \cdot T_{obs}$.

4. Experimental setup

4.1. Test specimen

The test specimen used in the present investigation is a cylindrical mild steel sample with an outer diameter of 50 mm, an inner diameter of 42 mm, and a height of 70 mm. The specimen contains a single artificial defect located on the inner surface, extending circumferentially over a height of 10 mm along the axial direction. The defect depth varies gradually along the circumferential direction from 1 mm to 4 mm, enabling simultaneous evaluation of defect-depth sensitivity and spatial localisation capability across a continuous range of subsurface material-loss conditions. A schematic representation of the specimen geometry and defect configuration is shown in figure 3.

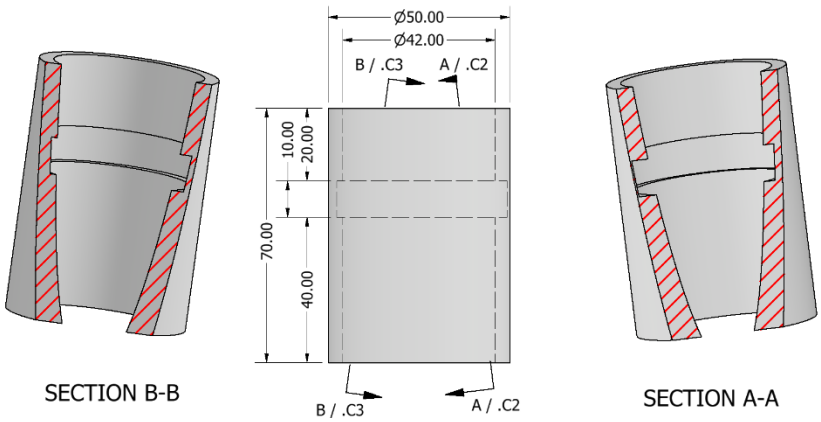

Figure 3. Schematic representation of the cylindrical mild steel specimen showing specimen geometry, defect dimensions, and circumferential variation in subsurface material-loss depth

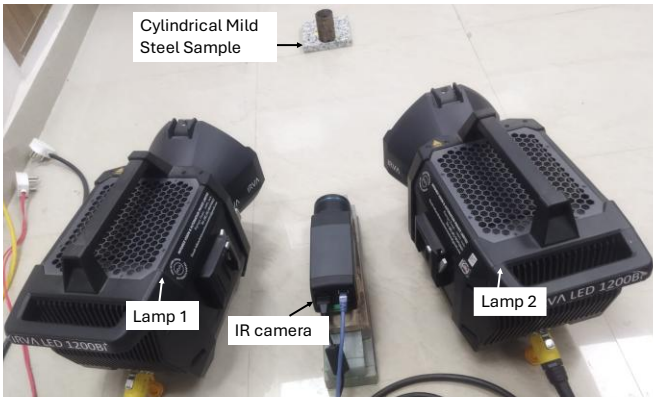

Figure 4. Experimental setup for active infrared thermographic inspection using LED-based excitation with tunable correlated colour temperature (CCT) and infrared thermal-response acquisition using an IR camera.

4.2. Instrumentation

The experimental setup for active infrared thermographic inspection used in this work including excitation control, data acquisition, and post-processing software, was designed and developed by InfraRed Vision & Automation Pvt. Ltd., Rupnagar, Punjab, India-140001 is illustrated in figure 4. It comprises an LED-based thermal excitation system and an infrared camera for acquiring thermal responses from the specimen surface. Two LED-based heating sources provided thermal excitation, each rated at 1200 W peak power, ensuring sufficient, approximately uniform illumination of the cylindrical specimen surface. The excitation system permits controlled variation of CCT across five discrete settings ranging from 2800 K to 6000 K in increments of 800 K, in accordance with the LED excitation model.

The thermal response of the specimen surface was recorded using a FLIR A655sc infrared camera operating in the long-wave infrared (LWIR) spectral range of 7.5–14 µm. The camera features a detector array resolution of 640 × 480 pixels, a noise-equivalent temperature difference (NETD) below 50 mK, a measurement temperature range of −40°C to 650°C, and a maximum frame acquisition rate of 50 Hz.

4.3. Experimental conditions

All experiments were conducted under controlled ambient conditions to minimise the influence of environmental disturbances, including airflow variations and ambient temperature fluctuations. Sufficient time intervals were maintained between successive measurements to ensure thermal equilibrium of the specimen before each experiment.

For pulsed thermography (PT) experiments, the specimen surface was subjected to a finite-duration thermal pulse generated using the LED excitation system. Experiments were performed at five discrete correlated colour temperature (CCT) settings: 2800 K, 3600 K, 4400 K, 5200 K, and 6000 K. Each experiment employed an excitation duration of 50 s, followed by thermal-response acquisition over a total observation duration of 100 s. Thermal data were recorded at a sampling rate of f_s=30 Hz for all experiments.

4.4. Experimental procedure

For each CCT condition, PT experiments were conducted on the same specimen under identical ambient conditions. Following each experiment, the acquired thermal sequence $T(x, y, t)$, $t \in [0, T_{obs}]$, was transferred for signal processing in accordance with the previously described framework. Zero-mean preprocessing was applied before FDP, TDP, and CCC analyses. Defect characterisation was subsequently evaluated through best-contrast-frame analysis, single-pixel profile (SPP) temporal analysis, and slope-based thermal absorption analysis during both heating and cooling phases.

5. Result and discussion

To investigate the influence of correlated colour temperature (CCT) on transient thermal response behaviour, the acquired pulsed thermography sequences were evaluated through best-contrast thermogram analysis, single-pixel profile analysis, and dual-phase slope analysis.

5.1. Best contrast frame analysis

Representative best-contrast thermograms for all five CCT conditions under FDP, TDP, and CCC processing are presented in figure 5. For each processing approach, the frame exhibiting maximum defect-to-background contrast was selected.

During FDP processing, defect-induced phase contrast is observable within a narrow temporal window of approximately 7-8 frames. Since FDP extracts phase information from individual frequency components of the transient thermal response, only a limited portion of the defect-correlated thermal information contributes to the final phase representation at a given instant. Nevertheless, systematic variation in thermographic response intensity is observable across the investigated CCT range, reflecting the influence of CCT on the transient thermal response behaviour.

Under TDP processing, defect visibility extends over a larger number of frames by preserving the instantaneous phase evolution in the time domain. However, phase distributions oscillate across the full −π to +π range throughout the observation sequence, and decorrelation events at certain temporal instances reduce the consistency of defect representation. Variations in CCT remain observable through changes in the intensity and spatial extent of the defect-induced phase signatures.

Among the investigated processing approaches, CCC produces the most spatially coherent and temporally persistent defect representation. By accumulating excitation-correlated thermal response over the full observation duration, CCC enhances defect visibility and produces the clearest distinction between defective and non-defective regions across all CCT conditions. The influence of CCT on thermographic response intensity is most clearly noticeable in the CCC thermograms owing to their superior spatial coherence and improved contrast stability.

Across all three processing approaches, thermographic response intensity increases progressively with increasing CCT, indicating enhanced transient thermal response at higher CCT conditions.

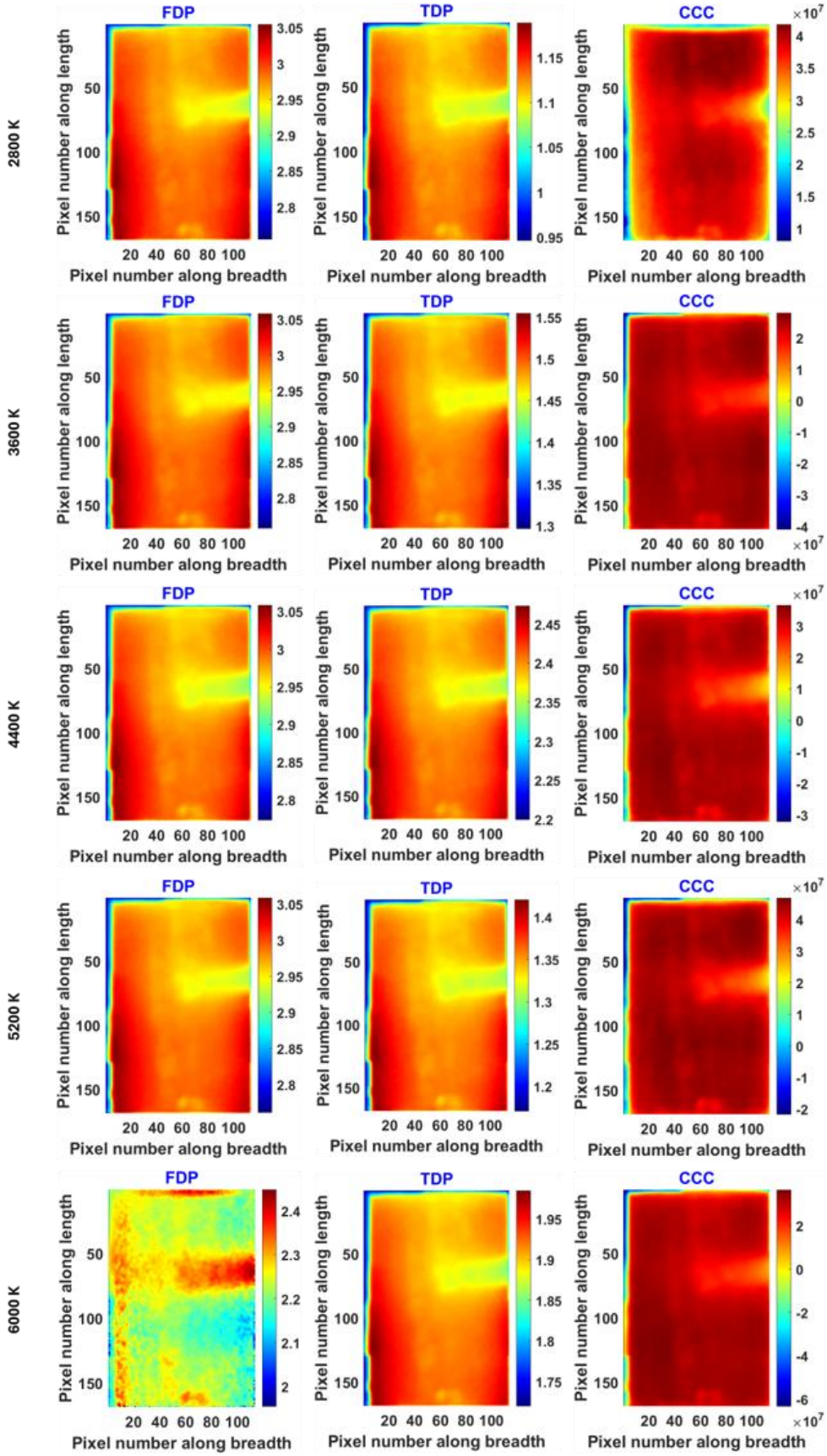

Figure 5. Representative best-contrast frames comparison obtained under PT for all investigated CCT conditions using FDP, TDP, and CCC processing.

5.2. Single pixel profile analysis

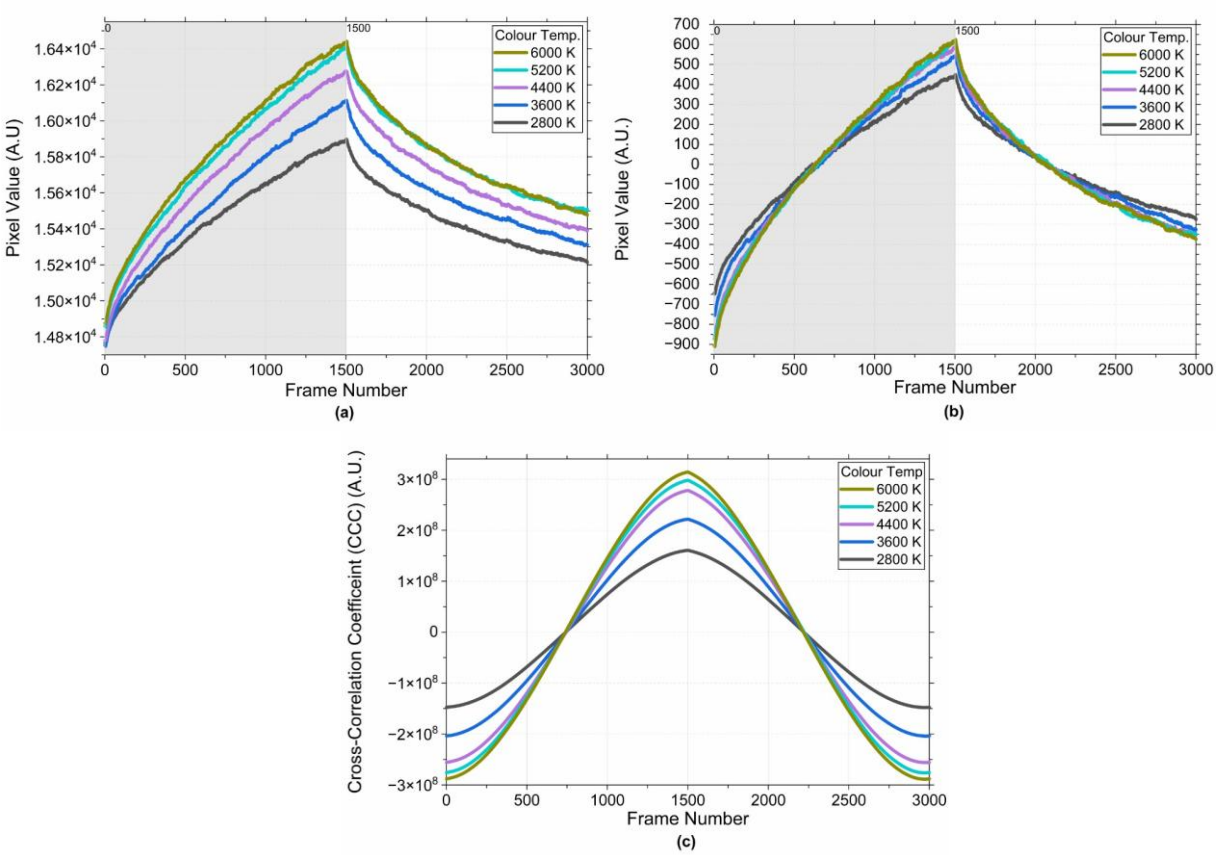

Figure 6. (a) raw, (b) mean-removed, and (c) CCC-based single-pixel profiles (SPPs) at the representative defect pixel under PT for all five CCT conditions (2800–6000 K)

Single-pixel profile analysis was performed at a representative pixel designated within the defective region of the specimen. Raw, zero-mean, and CCC-based temporal profiles for all five CCT conditions are presented in figure 6(a), figure 6(b),and figure 6(c). The grey-highlighted region identifies the heating phase (frames 0-1500) used for heating-slope computation; the remaining portion of the temporal sequence constitutes the cooling phase (frames 1500-3000) used for cooling-slope analysis.

The raw temporal profiles exhibit the characteristic two-phase pulsed thermography response. During the heating phase (frames 0–1500), the surface temperature rises progressively as the LED excitation source deposits thermal energy. A systematic increase in the rate of temperature rise is observed with increasing CCT from 2800 K to 6000 K, reflecting greater absorbed thermal energy at the specimen surface at higher CCT settings. During the cooling phase (frames 1500-3000), the surface temperature decays monotonically as heat diffuses into the bulk material. The cooling profiles become progressively steeper with increasing CCT, directly confirming that a higher peak surface temperature was achieved at the end of the heating phase, a behaviour consistent with the CCT-dependent enhancement of surface thermal absorption.

Following zero-mean pre-processing, the slowly varying background thermal component is suppressed while the dynamic thermal variations at the defect pixel are preserved. The progressive CCT-dependent amplitude difference is retained in the zero-mean profiles, confirming that CCT-induced response enhancement is intrinsic to the defect-region transient response rather than an artefact of the background thermal field. The CCC-based profiles exhibit the most distinct temporal separation between CCT conditions. The correlation integral amplifies the CCT-induced response differences, producing clearly separated temporal profiles for each CCT setting, with progressively higher peak responses at higher CCT conditions across both the heating and cooling phases.

Across all three representations, raw, zero-mean, and CCC, the SPP analyses confirm that increasing CCT produces a systematic and progressive enhancement of absorbed thermal energy at the defect pixel, manifested as increasing response amplitude during the heating phase and increasingly steep decay during the cooling phase. CCC provides the most sensitive and visually distinct representation of these CCT-induced variations.

5.3. Slope-based thermal absorption analysis

To quantitatively assess the influence of CCT on surface thermal energy absorption, a linear-fitting slope analysis of the raw pixel temperature profile was performed for both the heating (frames 0–1500) and cooling (frames 1500–3000) phases. The slope of the surface temperature rise during the heating phase is directly proportional to the rate of thermal energy absorption at the specimen surface. The cooling-phase slope characterises the subsequent thermal decay as heat diffuses into the bulk material; a steeper negative slope indicates a higher peak surface temperature was reached at the end of the heating phase, providing independent confirmation of the heating-phase findings. Together, the dual-phase slopes provide a comprehensive and physically grounded characterisation of CCT-dependent thermal coupling at the specimen surface.

Heating and cooling phase slopes computed for both raw and zero-mean thermal responses are summarised in Table 1. For the raw thermal response, the heating-phase slope increases monotonically with CCT, rising from 0.681 ± 0.003 at 2800 K to 0.939 ± 0.004 at 6000 K, an overall increase of 37.9% across the investigated range. The cooling-phase slope becomes progressively more negative over the same range, from −0.369 ± 0.002 at 2800 K to −0.525 ± 0.004 at 6000 K, corresponding to a 42.1% increase in the cooling response steepness, which is physically consistent with the progressively higher peak surface temperatures observed at elevated CCT settings.

The rate of slope increase diminishes at higher CCT values. The heating-phase slope increment between 2800 K and 3600 K is substantially larger than that between 5200 K and 6000 K, and the same pattern is reproduced in the cooling-phase data, indicating that surface thermal absorption approaches a saturation regime within the upper portion of the investigated CCT range for the mild steel specimen.

A consistent CCT-dependent trend is observed in the zero-mean representation across both heating and cooling phases. The heating-phase slope increases progressively with CCT, and the cooling-phase slope becomes increasingly negative, confirming that the CCT-dependent thermal response behaviour is preserved following background suppression and is therefore intrinsic to the defect-region transient response rather than an artefact of the slowly varying background thermal field.

The monotonic behaviour observed independently across both heating and cooling phase metrics, and its consistent reproduction across both raw and zero-mean representations, provides unambiguous quantitative confirmation that increasing CCT systematically enhances surface thermal energy absorption under pulsed thermographic excitation of mild steel.

Table 1. Heating and cooling-phase slope analysis of raw and mean-removed (MR) single-pixel thermal responses under pulsed thermography for all investigated correlated colour temperature (CCT) conditions.

Slope analysis of raw pixel profile for pulse thermography (PT)				
CCT	Heating Phase (0:1500 frames)		Cooling Phase (1500:3000 frames)	
	Slope (Raw)	Slopes (Mean Removed)	Slope (Raw)	Slopes (Mean Removed)
2800 K	**0.68064** ± 0.00268	0.65453 ± 0.00268	**-0.36927** ± 0.00239	-0.39538 ± 0.00239
3600 K	**0.81566** ± 0.00273	0.7709 ± 0.00273	**-0.42422** ± 0.00289	-0.46898 ± 0.00289
4400 K	**0.89667** ± 0.00350	0.86052 ± 0.0035	**-0.48535** ± 0.00308	-0.5215 ± 0.00308
5200 K	**0.93000** ± 0.00354	0.88847 ± 0.00354	**-0.50505** ± 0.0034	-0.54658 ± 0.0034
6000 K	**0.93892** ± 0.00384	0.91664 ± 0.00384	**-0.52471** ± 0.00353	-0.54698 ± 0.00353

6. Conclusion

This study presented a systematic investigation into the influence of correlated colour temperature (CCT) on subsurface defect characterisation in LED-based pulsed thermography. Experiments were conducted on a cylindrical mild steel specimen containing controlled subsurface material loss using five discrete CCT conditions ranging from 2800 K to 6000 K. Acquired thermal sequences were analysed using Frequency Domain Phase (FDP), Time Domain Phase (TDP), and Cross-Correlation Coefficient (CCC) processing together with single-pixel temporal analysis and dual-phase slope-based thermal-response evaluation.

Among the investigated processing approaches, CCC consistently produced superior defect representation compared to FDP and TDP, with improved spatial coherence, enhanced temporal persistence, and clearer separation of the defect signal across all CCT conditions. In contrast, the phase-domain approaches exhibited limited and temporally inconsistent defect behaviour during transient thermal evolution.

Dual-phase slope analysis quantitatively established that increasing CCT systematically enhances transient thermal response behaviour. The heating-phase slope increased by approximately 37.9% between 2800 K and 6000 K, while the cooling-phase slope exhibited an approximately 42.1% reduction over the same range. Similar monotonic trends were observed in both the raw and zero-mean representations, confirming that the CCT-dependent behaviour is preserved after preprocessing.

The rate of slope variation decreased at higher CCT conditions, with comparatively smaller slope changes observed above 5200 K for the investigated mild steel specimen. Overall, the findings establish correlated colour temperature as a physically significant and practically controllable excitation parameter capable of influencing transient thermal response and defect visibility in LED-based pulsed thermographic inspection.

References

[1] Xavier. Maldague, «*Theory and practice of infrared technology for nondestructive testing*.» Wiley, 2001.

[2] P. J. Shull, «*Nondestructive Evaluation*.» CRC Press, 2002.

[3] Charles. Hellier, «*Handbook of nondestructive evaluation*.» McGraw-Hill, 2013.

[4] D. L. Balageas, «Defense and illustration of time-resolved pulsed thermography for NDE,» *Quant. Infrared Thermogr. J.*, vol. 9, no. 1, pp. 3–32, Jun. 2012.

[5] C. Ibarra-Castanedo and X. Maldague, «Pulsed phase thermography reviewed,» *Quant. Infrared Thermogr. J.*, vol. 1, no. 1, pp. 47–70, Jun. 2004.

[6] V. P. Vavilov and D. D. Burleigh, «Review of pulsed thermal NDT: Physical principles, theory and data processing,» *NDT and E International*, vol. 73, pp. 28–52, Jul. 2015.

[7] N. P. Avdelidis, B. C. Hawtin, and D. P. Almond, «Transient thermography in the assessment of defects of aircraft composites,» *NDT & E International*, vol. 36, no. 6, pp. 433–439, Sep. 2003.

[8] C. Ibarra-Castanedo *et al.*, «Comparative Study of Active Thermography Techniques for the Nondestructive Evaluation of Honeycomb Structures,» *Research in Nondestructive Evaluation*, vol. 20, no. 1, pp. 1–31, Jan. 2009.

[9] C. Meola and G. M. Carlomagno, «Recent advances in the use of infrared thermography,» *Meas. Sci. Technol.*, vol. 15, no. 9, pp. R27–R58, Sep. 2004.

[10] C. Ibarra-Castanedo, D. González, M. Klein, M. Pilla, S. Vallerand, and X. Maldague, «Infrared image processing and data analysis,» *Infrared Phys. Technol.*, vol. 46, no. 1–2, pp. 75–83, Dec. 2004.

[11] H. S. Carslow, J. C. Jaeger, and J. E. Morral, «Conduction of Heat in Solids, Second Edition,» *J. Eng. Mater. Technol.*, vol. 108, no. 4, pp. 378–378, Oct. 1986.

[12] M. Necati. Özışık, «*Heat conduction*.» Wiley, 1993.

[13] Darryl. Almond and Pravin. Patel, «*Photothermal science and techniques*.» Chapman & Hall, 1996.

[14] D. P. Almond and S. K. Lau, «Defect sizing by transient thermography. I. An analytical treatment,» *J. Phys. D Appl. Phys.*, vol. 27, no. 5, pp. 1063–1069, May 1994.

[15] G. Dua, R. Mulaveesala, P. Mishra, and J. kaur, «InfraRed image correlation for non-destructive testing and evaluation of delaminations in glass fibre reinforced polymer materials,» *Infrared Phys. Technol.*, vol. 116, 2021.

[16] A. V. Oppenheim and R. W. . Schafer, «*Discrete-time signal processing*.» Pearson, 2010.

[17] B. Boashash, «Estimating and interpreting the instantaneous frequency of a signal. I. Fundamentals,» *Proceedings of the IEEE*, vol. 80, no. 4, pp. 520–538, Apr. 1992.

[18] S. K. Bhambhu, V. Arora, and R. Mulaveesala, «Matched Filter-Based Post Processing Approach for Active Infrared Thermography for Nondestructive Testing and Evaluation of Carbon Fibre Reinforced Polymer Materials,» *Russian Journal of Nondestructive Testing*, vol. 61, no. 6, pp. 704–714, Jun. 2025.

[19] S. Tuli and R. Mulaveesala, «Defect detection by pulse compression in frequency modulated thermal wave imaging,» *Quant. Infrared Thermogr. J.*, vol. 2, no. 1, pp. 41–54, 2005.

[20] R. Mulaveesala and S. Tuli, «Implementation of frequency-modulated thermal wave imaging for non-destructive sub-surface defect detection,» *Insight - Non-Destructive Testing and Condition Monitoring*, vol. 47, no. 4, pp. 206–208, Apr. 2005.

[21] N. Tabatabaei and A. Mandelis, «Thermal-wave radar: A novel subsurface imaging modality with extended depth-resolution dynamic range,» *Review of Scientific Instruments*, vol. 80, no. 3, Mar. 2009.